JACS
JOURNAL OF THE AMERICAN CHEMICAL SOCIETY

Article

pubs.acs.org/JACS

Synthesis, Internal Structure, and Formation Mechanism of Monodisperse Tin Sulfide Nanoplatelets

Antoine de Kergommeaux,[*,†,‡,§,⊗] Miguel Lopez-Haro,[∥,⊥] Stéphanie Pouget,[∥,⊥] Jian-Min Zuo,[#] Colette Lebrun,[▽,¶] Frédéric Chandezon,[†,‡,§] Dmitry Aldakov,[†,‡,§] and Peter Reiss[*,†,‡,§]

[†]Univ. Grenoble Alpes, INAC-SPrAM, F-38054 Grenoble Cedex 9, France
[‡]CNRS, SPrAM, F-38054 Grenoble Cedex 9, France
[§]CEA, INAC-SPrAM, F-38054 Grenoble Cedex 9, France
[∥]Univ. Grenoble Alpes, INAC-SP2M, F-38054 Grenoble Cedex 9, France
[⊥]CEA INAC-SP2M, F-38054 Grenoble Cedex 9, France
[#]Department of Materials Science and Engineering, University of Illinois, Urbana−Champaign, Urbana, Illinois 61801, United States
[▽]Univ. Grenoble Alpes, INAC-SCIB, F-38054 Grenoble Cedex 9, France
[¶]CEA INAC-SCIB, F-38054 Grenoble Cedex 9, France

Supporting Information

ABSTRACT: Tin sulfide nanoparticles have a great potential for use in a broad range of applications related to solar energy conversion (photovoltaics, photocatalysis), electrochemical energy storage, and thermoelectrics. The development of chemical synthesis methods allowing for the precise control of size, shape, composition, and crystalline phase is essential. We present a novel approach giving access to monodisperse square SnS nanoplatelets, whose dimensions can be adjusted in the range of 4−15 nm (thickness) and 15−100 nm (edge length). Their growth occurs via controlled assembly of initially formed polyhedral seed nanoparticles, which themselves originate from an intermediate tetrachlorotin-oleate complex. The SnS nanoplatelets crystallize in the α-SnS orthorhombic herzenbergite structure (space group *Pnma*) with no evidence of secondary phases. Electron tomography, high angle annular dark field scanning transmission electron microscopy and electron diffraction combined with image simulations evidence the presence of ordered Sn vacancy rich (100) planes within the SnS nanoplatelets, in accordance with their slightly S-rich composition observed. When using elemental sulfur instead of thioacetamide as the sulfur source, the same reaction yields small (2−3 nm) spherical SnS_2 nanoparticles, which crystallize in the berndtite 4H crystallographic phase (space group *P*3*m*1). They exhibit quantum confinement (E_g = 2.8 eV vs 2.2 eV in the bulk) and room temperature photoluminescence. By means of electrochemical measurements we determined their electron affinity EA = −4.8 eV, indicating the possibility to use them as a substitute for CdS (EA = −4.6 eV) in the buffer layer of thin film solar cells.

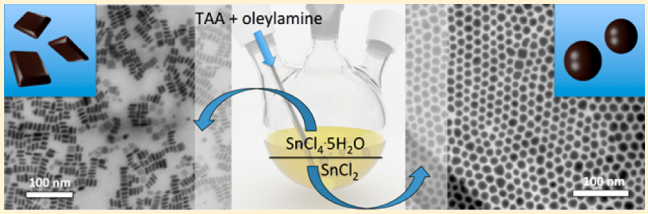

INTRODUCTION

The shape control of chemically synthesized colloidal semiconductor nanostructures has undergone fast progress during the past 15 years. Today many synthesis routes exist for 1D nanostructures (nanorods),[1] branched systems (e.g., tetrapods,[2] octapods,[3] hyperbranched nanocrystals[4]) and 2D nanostructures (nanosheets,[5] nanoplatelets[6,7]). The main interest of controlling the shape arises from the resulting novel optical, electronic and assembly properties of these complex nanostructures. To give an example, the precisely controlled thickness of CdSe nanoplatelets in a range of a few monolayers gives rise to very sharp features in the absorption and photoluminescence spectra.[6] This is a consequence of the strong quantum confinement in one direction of space, while the other two directions are not confined, similar to epitaxially grown quantum wells.[8] 1D and 2D semiconductor nanostructures open furthermore new horizons for the generation of ordered architectures through self-assembly into superstructures.[9−12] Using this strategy, metamaterials can be obtained, which exhibit novel collective behavior such as for example anisotropic transport properties, depending on the orientation of the individual nanocrystals within the solid.[13−15] 2D nanostructures are expected to show distinct advantages over spherical and rodlike geometries in terms of charge transfer and transport in layered devices, which contain a thin film of semiconductor nanocrystals as the active material (e.g., field-effect transistors, light-emitting diodes, photovoltaic cells or photodetectors).

Tin^{II} sulfide is currently investigated as low cost, earth abundant and environmentally benign solar light harvesting material for thin-film photovoltaic cells as an alternative to

Received: May 29, 2015
Published: July 22, 2015

DOI: 10.1021/jacs.5b05576
J. Am. Chem. Soc. 2015, 137, 9943−9952

CdTe and CIGS.[16,17] Other areas of potential application include photodetectors,[18,19] anode materials for Li-ion batteries,[20−22] thermoelectrics[23] and photocatalysis.[19,24] Considering solar energy conversion, SnS presents an indirect band gap of 1.07 eV with an effective absorption onset at around 1.4−1.5 eV[25] and a high absorption coefficient ($\alpha > 10^4$ cm^{-1}).[26] The material shows intrinsic p-type doping through the formation of Sn vacancies acting as shallow acceptors.[25] The solar cell power conversion efficiency has progressed significantly in the past few years reaching currently 4.4%.[27] Meanwhile, theoretical predictions indicate that efficiencies up to 24% should be reachable in a single junction device through the choice of suitable growth conditions and more appropriate n-type materials.[25,28] On the side of the SnS absorber the formation of deep trap states resulting from S vacancies (V_s) or Sn-on-S antisite defects (Sn_S) should be avoided by choosing S-rich growth conditions. At the same time, in order to prevent formation of secondary S-rich phases like Sn_2S_3 or SnS_2, the sulfur excess has to be controlled in narrow limits.[28] In this context the growth of SnS in form of colloidal nanocrystals of precisely controlled size, shape, composition and crystal structure, which can be subsequently processed as thin films from solution, offers many advantages.[29] Bulk SnS, naturally occurring as mineral herzenbergite, crystallizes in the orthorhombic crystal system. The atoms adopt a distorted NaCl structure with nominally octahedral coordination, characterized by two-atom-thick Sn−S layers in *b* and *c* directions, with larger nearest-neighbor distances and hence weaker bonding in *a* direction.[30] Therefore, SnS is intrinsically prone to the formation of anisotropic nanostructures and synthesis methods yielding a large variety of morphologies have been reported: spherical or close-to-spherical SnS nanoparticles,[31−38] tetrahedral particles,[39,40] nanocubes,[33,40] nanorods,[21] nanoribbons,[18,19,22] nanoflowers[20,36,41] and nanosheets.[5,33,36,41] In many of these works the obtained X-ray data differs from the pattern expected for the above-mentioned orthorhombic α-SnS phase. This discrepancy is generally explained by the coexistence of the metastable zinc blende polymorph of SnS.[18,22,34−36,38,39] To the contrary, Schaak et al. recently found that the observed diffraction patterns could be fully indexed using a pseudotetragonal modification of α-SnS, showing unit cell expansion along the *a* and *b* axes and contraction along *c* axis.[33]

Here we describe a new method for the synthesis of 2D SnS nanoplatelets using for the first time the Sn^{IV} precursor tin tetrachloride pentahydrate, which is reacted in the presence of trioctylphosphine and oleic acid with thioacetamide (TAA). In this reaction, first a tetrachlorotin-oleate complex is formed, which has been identified by mass spectrometry. In the second step, hydrogen sulfide generated by the thermal decomposition of TAA serves as the sulfur source and reducing agent of the tin precursor. The developed synthesis yields monodisperse square-shaped platelets of precisely controlled dimensions showing an edge length in the range of 15−100 nm and a thickness of 4−15 nm. The nanoplatelets crystallize in the orthorhombic α-SnS phase (space group *Pnma*) and exhibit slightly S-rich composition (Sn = 48.5%, S = 51.5%). High-resolution transmission electron microscopy in high angle annular dark field configuration and comparison with image simulations reveal the presence of ordered Sn vacancies rich (100) planes within the SnS nanoplatelets. By varying the reaction parameters we identified that their growth takes place via the nucleation of isotropic primary seed nanoparticles, followed by their assembly into 2D nanostructures. Finally, when using elemental sulfur instead of TAA as the sulfur source, the same reaction yields small (2−3 nm) SnS_2 nanoparticles, showing interesting optical and electronic properties.

EXPERIMENTAL SECTION

Chemicals. $SnCl_4{\cdot}5H_2O$ (98%), $SnCl_2$ (99%), 1-octadecene (90%), oleic acid (80−90%), thioacetamide (>99.0%), sulfur (99.9%), oleylamine (70%), anhydrous chloroform and ethanol have been purchased from Sigma-Aldrich, trioctylphosphine (90%) from Fluka.

SnS Nanoplatelets Synthesis. $Tin^{(IV)}$ chloride pentahydrate ($SnCl_4{\cdot}5H_2O$, 35−350 mg, 0.1−1 mmol) is mixed in a three neck flask with 1-octadecene (ODE, 3−18 mL), trioctylphosphine (TOP, 1 mL, 2.24 mmol) and oleic acid (OA, 1 mL, 3.17 mmol) inside a glovebox under argon atmosphere. The mixture is then degassed under primary vacuum (0.05 mbar) at 100 °C during 1 h. The sulfur precursor is prepared by dissolving thioacetamide (TAA, 7.5−150 mg, 0.1−2 mmol) in oleylamine (OLA, 2 mL, 6 mmol) to form a 0.05−1 M solution. It should be noted that he TAA-OLA solution has to be freshly prepared prior to synthesis in order to avoid the decrease of the sulfur concentration with time due to the formation of volatile H_2S gas. The flask containing the tin salt solution is backfilled with argon, heated to 150 °C and kept at this temperature for 1 h. Next, the TAA-OLA solution is swiftly injected into the flask under vigorous stirring. An instantaneous color change from transparent to black takes place and the temperature is kept for 3−60 min at 150 °C before cooling down with an ice bath. The SnS nanoplatelets are purified by precipitation with a chloroform/ethanol mixture (1:2 vol:vol), centrifugation (9000 rpm, 2 min) and redispersion in 10 mL of chloroform leading to a stable colloidal solution of dark brown color; for small size nanoplatelets (e.g., 7 nm thick, 17 nm edge length) no precipitation is detected even after 2 years storage at ambient temperature.

Synthesis Parameters for 7 × 17 nm SnS Nanoplatelets (cf. Figure 1b). $SnCl_4{\cdot}5H_2O$: 350 mg (1 mmol), ODE: 3 mL, TOP: 1 mL, OA: 1 mL, TAA: 150 mg (2 mmol), OLA: 2 mL, reaction time at 150 °C: 10 min.

Spherical SnS Nanocrystals Synthesis. The synthesis of spherical SnS nanocrystals (NCs) follows the protocol A described in our previous work.[34] For direct comparison with the nanoplatelet synthesis, the same conditions have been chosen as detailed above, while replacing $SnCl_4{\cdot}5H_2O$ by anhydrous $SnCl_2$.

Synthesis of ∼3 nm SnS_2 Nanoparticles. $SnCl_4{\cdot}5H_2O$ (350 mg, 1 mmol) was loaded into a 50 mL three-neck flask with ODE (3 mL, 15.6 mmol), TOP (1 mL, 2.24 mmol) and OA (1 mL, 3.17 mmol) and degassed under primary vacuum during 1 h at 100 °C. Next the temperature was increased to 130 °C and a solution containing sulfur (64 mg, 2 mmol) in OLA (2 mL, 6 mmol) was swiftly injected under vigorous stirring. The reaction was left at this temperature for 5 min and then cooled down to room temperature with an ice bath. Ethanol (15 mL) was added to precipitate the NCs, which were collected by centrifugation at 8000 rpm for 2 min. After dispersion in 5 mL of chloroform, the NCs were purified a second time using the same procedure and finally dispersed in 5 mL of chloroform to form stable colloidal solutions of yellow-orange color.

Characterization Methods. Scanning electron microscopy (SEM) and scanning electron transmission microscopy (STEM) images were acquired with a ZEISS Ultra 55+ Electron Microscope. For STEM, the NCs were drop-cast on carbon coated copper grids (Ted Pella) and dried under vacuum. Powder X-ray diffraction has been carried out on a Panalytical X'Pert powder diffractometer equipped with a copper anode ($\lambda K\alpha 1$ = 1.5406 Å, $\lambda K\alpha 2$ = 1.5444 Å) and an X'Celerator 1D detector. It was configured in Bragg−Brentano geometry, with a variable divergence slit on the primary beam path and a set of antiscattering slits positioned before and after the sample. Axial divergence was limited by 0.02 rad Soller slits.

DOI: 10.1021/jacs.5b05576
J. Am. Chem. Soc. 2015, 137, 9943−9952

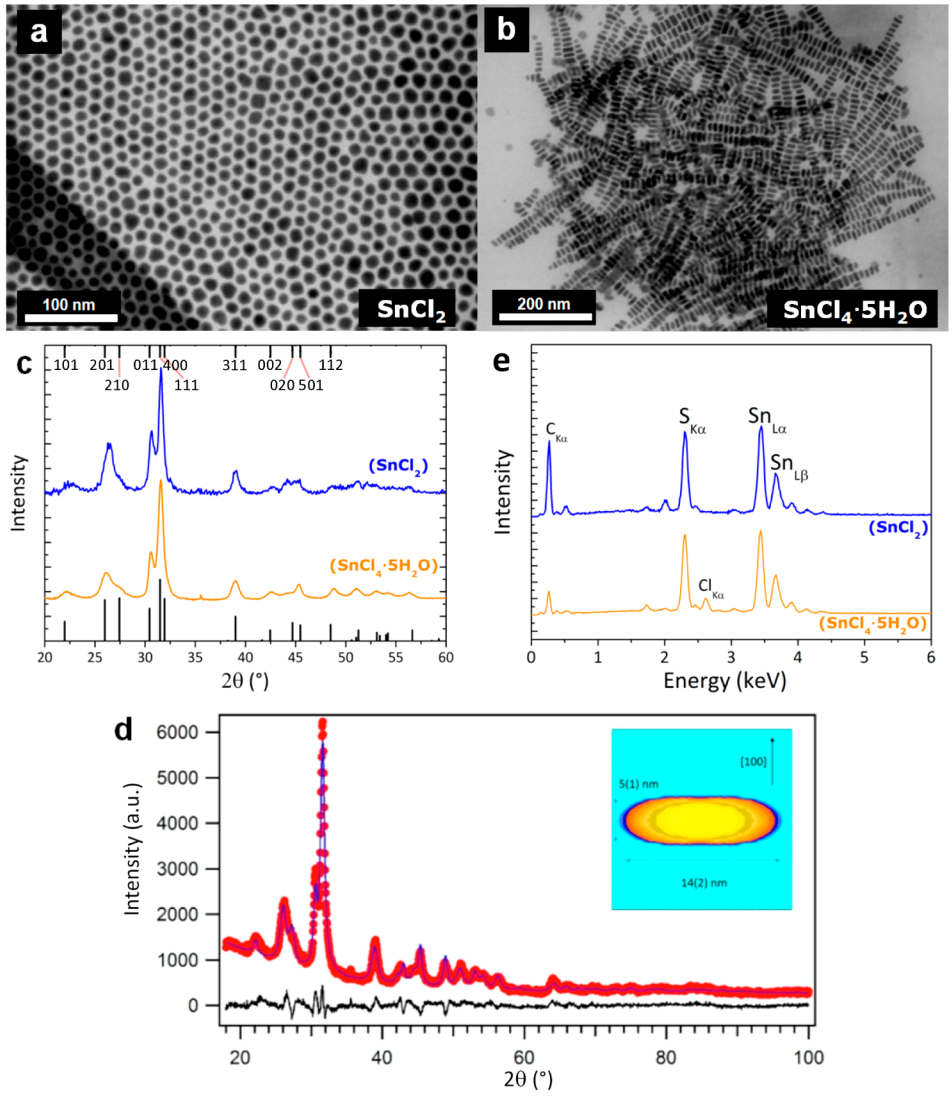

Figure 1. STEM images of (a) spherical NCs synthesized with $SnCl_2$ as tin precursor; (b) platelet-shaped SnS NCs synthesized with $SnCl_4{\cdot}5H_2O$. (c) Powder X-ray diffractograms for both types of NCs (Cu Kα, λKa1 = 1.5406 Å; λKa2 = 1.5444 Å). The vertical lines indicate the expected peak positions for the orthorhombic Herzenbergite structure (indexed on top). (d) Rietveld refinement of the X-ray diffractogram of the nanoplatelets (red: experimental data; blue: calculated pattern; black: difference plot). Inset: average particle shape deduced from the refined peak broadening. (e) EDX measurements.

Electron tomography analysis was performed in the high angle annular dark field scanning transmission electron microscopy (HAADF-STEM) mode on a FEI TITAN 80−300 LB electron microscope equipped with a probe Cs-corrector, operating at 200 kV and using a Fischione 2020 ultrahigh-tilt tomography holder. Before recording a series of images, the aberrations of the condenser lenses were corrected up to second-order using the Zemlin tableau. A convergence angle of 10 mrad was used in order to improve the depth of focus. The data collections were performed by tilting the specimen around a single axis perpendicular to the electron beam in a range of −70° to +62° every 2°. The registered tilt series were aligned using the FEI Inspect 3D software and reconstructed using software written in MATLAB. In particular, 50 iterations were used using SIRT algorithm. The reconstructed volumes were thereafter processed using the Avizo 7.0 Fire edition and Fiji software.

The aberration-corrected HAADF-STEM images were recorded using same FEI TITAN 80−300 LB electron microscope equipped with a probe Cs-corrector, operating at 300 kV. The aberrations of the condenser lenses were corrected up to third-order using the Zemlin tableau to obtain a sub-Angstrom electron probe. A condenser aperture of 50 μm and a 130 mm camera length were used, yielding an electron probe with a convergence semiangle of 18 mrad. The SnS structural models used in our HR-HAADF image simulation studies were built with RHODIUS, a computer program developed at Cadiz University.[42] TEMSIM software was used for HR-HAADF image simulations.[43] The following electro-optical parameters were used in accordance with the experiment: accelerating voltage = 300 kV, C_3= 0.005 mm, C_5 = 32 mm, Δf = −3 nm, convergence angle = 18 mrad and ADF collection angle = 51−353 mrad. The HAADF image simulations were convoluted with a 0.13 nm fwhm Gaussian.

The mass spectra were recorded on a LXQ type THERMO SCIENTIFIC spectrometer, equipped with an electrospray ionization source and a linear-trap detector. Solutions were injected in the spectrometer at 10 μLmin^{-1} flow rate. Ionization voltage and capillary temperature were set at about 5 kV and 180 °C respectively. The data were acquired in negative mode with an injection time of 5−200 ms. The LXQ calibration (m/z 50−2000) was achieved according to the standard calibration procedure from the manufacturer (mixture of caffeine, MRFA and Ultramark 1621).

RESULTS AND DISCUSSION

1. Crystallographic Properties of SnS Nanoplatelets. Tin^{IV} tetrachloride pentahydrate ($SnCl_4{\cdot}5H_2O$) yields square

DOI: 10.1021/jacs.5b05576
J. Am. Chem. Soc. 2015, 137, 9943−9952

cuboid shaped $Sn^{II}S$ nanocrystals (NCs), termed for simplicity nanoplatelets, when reacted at 150 °C with a thioacetamide (TAA)/oleylamine (OLA) solution in the presence of trioctylphosphine (TOP) and oleic acid (OA) in 1-octadecene (ODE). When tin^{II} chloride ($SnCl_2$) is used as the tin precursor, the same reaction provides spherical/faceted SnS nanoparticles (Figure 1).

The latter exhibit an average diameter of 12 nm and a size distribution of 17%, while the square platelets have lateral dimensions of 17 ± 3.4 nm and a thickness of 6.9 ± 1.4 nm. They tend to self-assemble in lines by columnar stacking in the direction of their flat surfaces, which maximizes van der Waals interactions between them. This kind of assembly leads to edge-on orientation on the substrate (Figure 1b). Some individual face-on particles can also be observed next to these assemblies. At a first glance the X-ray diffractograms obtained with both types of NCs are consistent with the presence of the α-SnS orthorhombic herzenbergite crystalline phase, as reported for the bulk material (Figure 1c).[44] In the case of the spherical particles, Bragg peaks are hardly discernible for diffraction angles larger than 40°, indicating the presence of defects and/or disorder in the structure. A LeBail fit of the data assuming *Pnma* space group converged to the following lattice parameters: a = 11.32 ± 0.03 Å, b = 4.04 ± 0.01 Å, c = 4.23 ± 0.01 Å. In addition Rietveld analysis of the data recorded for the platelet-shaped NCs was performed using Fullprof software.[45] Microstructure effects were taken into account by linear combinations of spherical harmonics to model peak broadening. Figure 1d shows the result of the refinement together with the determined average NC's shape, which is coherent with STEM observations. The platelets are flattened along [100] direction with characteristic dimensions of the order of 5 and 14 nm. The lattice parameter values are close to those obtained for the spherical particles: a = 11.34 ± 0.03 Å, b = 4.00 ± 0.01 Å, c = 4.29 ± 0.01 Å. Site occupancies were refined; their values correspond to a stoichiometry of (Sn = 40%, S = 60%). However, this determination is not precise as various parameters affect the integrated intensities, which cannot be unambiguously disentangled due to the limited wealth of information contained in our data. Considering the different SnS cards of the ICDD PDF4 database, Debye−Waller factors were kept constant at 1.05 $Å^2$ and 0.95 $Å^2$ for Sn and S, respectively. Residual differences between measured and calculated patterns might be explained by the presence of defects in the structure. EDX measurements (Figure 1e) have been used to determine the stoichiometry of the nanoplatelets (Sn = 48.5%, S = 51.5%), which is very close to that of the spherical NCs (Sn = 48.6%, S = 51.4%). The close-to equimolar stoichiometry demonstrates that the tin precursor has been reduced during the reaction to form SnS NCs. Sn(IV) containing compounds would result in completely different stoichiometries (e.g., Sn_2S_3, SnS_2). We also note the very low intensity of the peak at 2 theta = 35°, characteristic of SnO_2.

In order to correlate more precisely morphology and crystallographic properties of the SnS nanoplatelets, high resolution electron microscopy and electron tomography have been performed. Figure 2a presents an aberration-corrected scanning transmission electron microscopy high angle annular dark field (STEM-HAADF) image of a single SnS nanocuboid, representative of the nanoparticles observed in the sample. The crystallographic information was extracted from the results of Fourier analysis. Thus, the spots lighting up in the digital diffraction patterns (DDPs) show the distances characteristic of

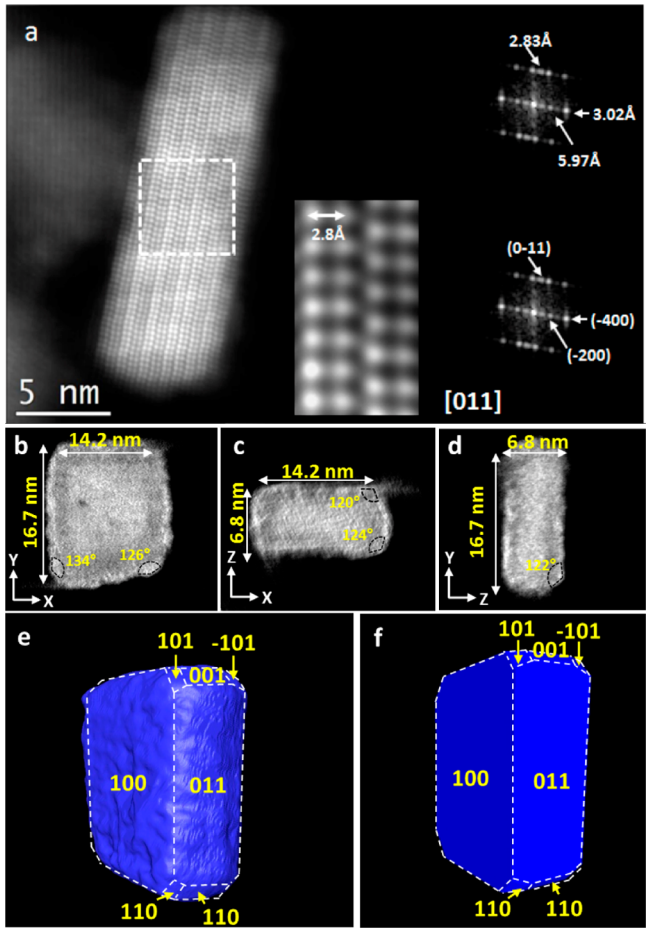

Figure 2. (a) Aberration-corrected scanning transmission electron microscopy high angle annular dark field (STEM-HAADF) image of a single SnS nanocuboid (edge view); enlarged region of the SnS nanocrystal showing the atomic columns; digital diffraction pattern (DDP) taken from the site marked with a square. (b−d) STEM-HAADF electron tomography: orthoslices extracted from the entire volume of a nanocrystal through (b) *xy* axis; (c) *xz* axis; (d) *yz* axis. (e) 3D surface rendering tomographic reconstruction of a single SnS nanoplatelet and (f) ideal model of the nanoplatelet according to the tomographic reconstruction with its lattice plane assignment.

(0−11) and (100) planes of an orthorhombic lattice in [011] orientation. This result is in full agreement with the results from X-ray analysis. The 3D observation of a nanostructure smaller than 50 nm is challenging using standard SEM and TEM techniques. Therefore, HAADF-STEM electron tomography series were performed on the same nanoplatelet by acquiring images form −70° to 62° each 2°. Afterward, they were aligned and reconstructed using the SIRT algorithm. Orthoslices (Figures 2b−d) extracted from the reconstructed volume of an isolated nanocuboid clearly show a well faceted structure, having lateral dimensions in concordance with the STEM images, i.e., edge length of 16.7/14.2 nm and thickness of 6.7 nm. Figure 2e displays the final reconstructed 3D surface rendering of the single SnS NC together with an ideal model, Figure 2f. In view of these images, the nanostructure can be described as a nonregular octagonal prism. We emphasize that the 3D reconstruction from electron tomography is in excellent agreement with the XRD results obtained from Rietveld analysis, specifically the platelet shape flattened along [100] direction.

DOI: 10.1021/jacs.5b05576
J. Am. Chem. Soc. 2015, 137, 9943−9952

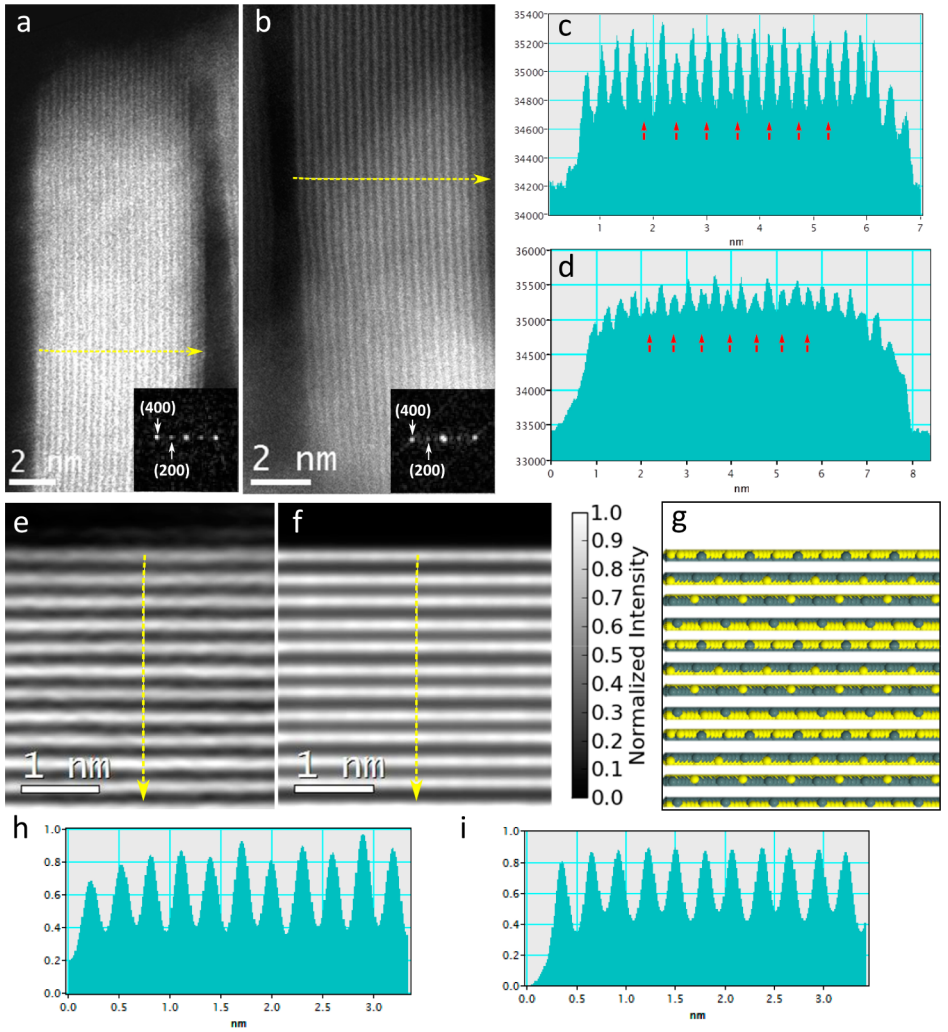

Figure 3. (a,b) Aberration-corrected HAADF images of two different SnS nanoplatelets on [011] off-zone axis systematic diffraction condition and corresponding power spectra (insets). (c,d) Intensity profiles corresponding to the lines marked on the HAADF images. Arrows in (c) and (d) indicate the Sn vacancy rich (100) planes. (e,f) Enlarged area of the experimental (e) and simulated (f) HAADF images. (g) Supercell of the stoichiometric crystal structure projected through the [011] zone axis considering a thickness of 13 nm and tilted 15°. (h,i) Intensity profiles corresponding to experimental and simulated HAADF images.

Two representative aberration-corrected HAADF-STEM images of square SnS nanoplatelets on [011] off-zone axis reveal a periodic modulation in image contrast (Figures 3a,b). This is emphasized by taking intensity profiles along the (100) planes (Figures 3c,d). In this imaging mode, the intensity varies with the square of the atomic number Z^2 and the thickness of the analyzed area.[46] It is worth mentioning that this periodically modulated contrast was found in *all* HAADF images of several tens of anisotropic SnS nanocrystals analyzed. To better understand this modulation, the normalized variations of the experimental HAADF intensity (Figure 3e) were compared to the projected potential of a structural model (Figure 3f) built using the crystallographic parameters of the average structure inferred by XRD in [011] zone axis and 15° tilted planes (Figure 3g). Clearly, the intensity variations from the model do not match the experimental ones and in particular do not display the modulation observed in the experiment (Figure 3h,i). Since the observed image intensity is dominated by the contributions from Sn atoms, the modulation must originate from a deviation of Sn concentration as compared to the average structural model. Previously, Vidal and co-workers have demonstrated by theoretical calculations and experiments that bulk SnS possesses a high concentration of Sn vacancy defects because of the small enthalpy of this defect formation.[25] Thus, our images suggest the presence of Sn vacancy (100) rich planes.

To get further information about the structure of the nanoplatelets at atomic scale, the spatial average technique was applied using the most advanced software on the basis of the analysis of atomically resolved images by means of template matching. Note that this image treatment allows us improving the resolution due to the reduction of noise.[47] Figure 4b illustrates the spatial average of the group of atomic columns of the nanocuboid of Figure 2. This image indicates that the atomic columns appear as elongated shape contrast whose intensity varies from site to site. Additionally, it should be pointed out that an extra intensity can be seen between the atomic columns (marked with an arrow). These characteristics appear more clearly in the intensity profile over the columns, Figure 4c. As for the nanocuboids on off-axis, to understand such features a simulated image of the projected structure on the [011] zone axis (Figure 4d) was compared to the

DOI: 10.1021/jacs.5b05576
J. Am. Chem. Soc. 2015, 137, 9943−9952

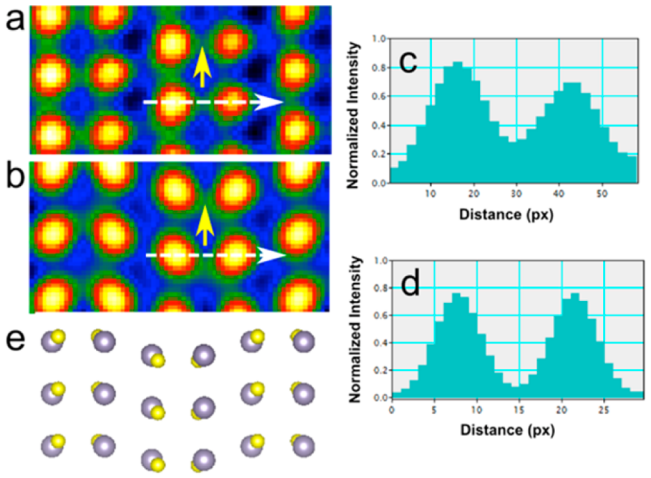

Figure 4. (a) Spatial averaged HAADF image of a group of atomic columns of the nanocuboid in Figure 2. (b) HAADF simulated image using the same electro-optical parameters as for the previous calculations in Figure 3. (c,d) Intensity profiles corresponding to the lines marked on the spatially averaged HAADF image (c) and simulated image (d). (e) Supercell of the crystal structure projected through the [011] zone axis (Sn: purple; S: yellow).

normalized intensity of the averaged image. The atomic columns present the same elongated shape as well as the extra intensity between them, although not as large as in the experimental image. To the contrary, the intensities of the atomic columns do not match as shows the intensity profile displayed in Figure 4e. The elongated shape is in agreement with the crystallographic positions of Sn and S: in the [011] projection of the orthorhombic lattice the S atoms are slightly shifted with respect to the Sn atoms (Figure 4d). On the other hand, the modulations found in the atomic columns allow us to confirm our previous analysis. Therefore, our experimental results are consistent with a high concentration of defects in the obtained SnS NCs. Furthermore, the observed periodic contrast modulations indicate an ordering of these defects. It can be expected that the density and organization of such features in the crystal lattice strongly influence the optoelectronic properties of SnS nanocrystals.

2. Influence of Reaction Parameters on Particle Morphology, Growth Mechanism. The synthesis of SnS nanoplatelets takes place in two steps: first, the complexation of the tin precursor in the presence of OA and TOP; second, the reaction with the sulfur precursor TAA to form SnS nanoparticles. By means of control experiments using only one of the complexing agents (either TOP or OA) we identified that both are required for the subsequent formation of SnS nanoplatelets. Oleate ligands act as complexing agent for Sn^{4+} ions, following the HSAB principle (hard base/hard acid couple). The neutral donor ligand TOP, on the other hand, is supposed to coordinate as a soft base preferentially Sn^{2+} ions present in the final nanoparticles. In the starting compound tin^{IV} tetrachloride pentahydrate, the tin ion is coordinated by four chlorine atoms and two water molecules, forming a slightly distorted octahedral coordination sphere.[48] The intermolecular packing is governed by hydrogen bonding implying further water molecules. By means of electrospray ionization (ESI) mass spectrometry we unambiguously identified the intermediate complex formed in the first stage of the reaction to be $SnCl_4$ coordinated with one oleate molecule (cf. Supporting Information). This indicates that the reduction of the tin precursor only takes place in the second stage, upon injection of the TAA/OLA solution. TAA thermally decomposes in organic solvents into acetonitrile and hydrogen sulfide, the latter acting as reducing agent for Sn^{IV} and sulfur source. The high chlorine content of the intermediate complex is expected to contribute to the formation of square platelets instead of isotropic spherical particles. As seen in the EDX data (Figure 1d and Supporting Information), the final product after purification still contains a significant amount of chlorine whereas almost no chlorine can be detected in the case of spherical nanoparticles obtained when using $SnCl_2$ as the tin precursor. We hypothesize that specific chlorine terminated crystal facets of the primary seed particles allow for a close interparticular contact during their 2D assembly.

With the goal to investigate the influence of the reaction parameters on the size and shape of the obtained nanoparticles

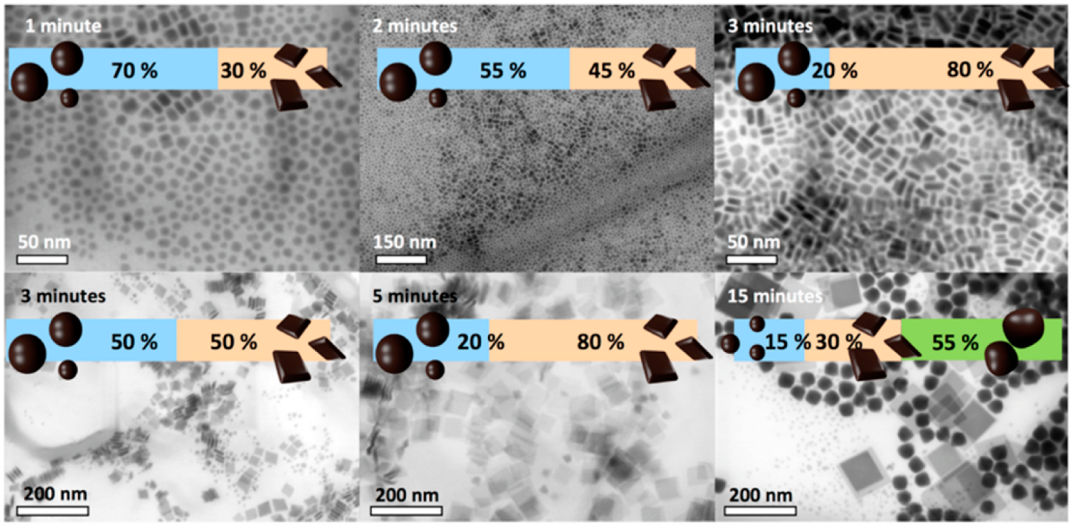

Figure 5. Top row: evolution of the shape with reaction time for high precursor concentration ([Sn] = 0.143 M, Sn:S ratio 1:2, T = 150 °C). The ratio of spherical particles and nanoplatelets is indicated. Bottom row: evolution when using low precursor concentration ([Sn] = 0.005 M, Sn:S ratio 1:5, T = 150 °C). The thickness of the platelets is 8 nm, the edge length 30 nm (3 min), 50 nm (5 min) and 100−150 nm (15 min), respectively.

DOI: 10.1021/jacs.5b05576
J. Am. Chem. Soc. 2015, 137, 9943−9952

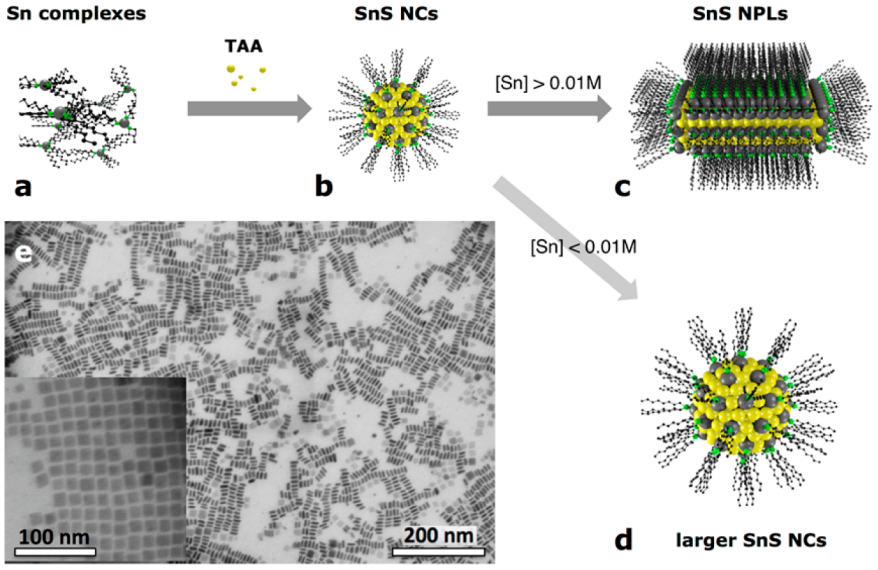

Figure 6. Growth mechanism of SnS square nanoplatelets (c) via the assembly of spherical seed nanoparticles (b) formed upon injection of the sulfur precursor into a solution of the complexed Sn precursor (a). The competing pathway (d) can be suppressed by proper choice of the reaction conditions, as shown in (e) where the following parameters have been used: [Sn] = 0.143 M, Sn:S ratio 3:1, T = 150 °C, reaction time 5 min, leading to monodisperse nanoplatelets with a thickness of 4.4 ± 0.5 nm and edge length of 14.4 ± 1.2 nm. (No size-selective precipitation is performed.)

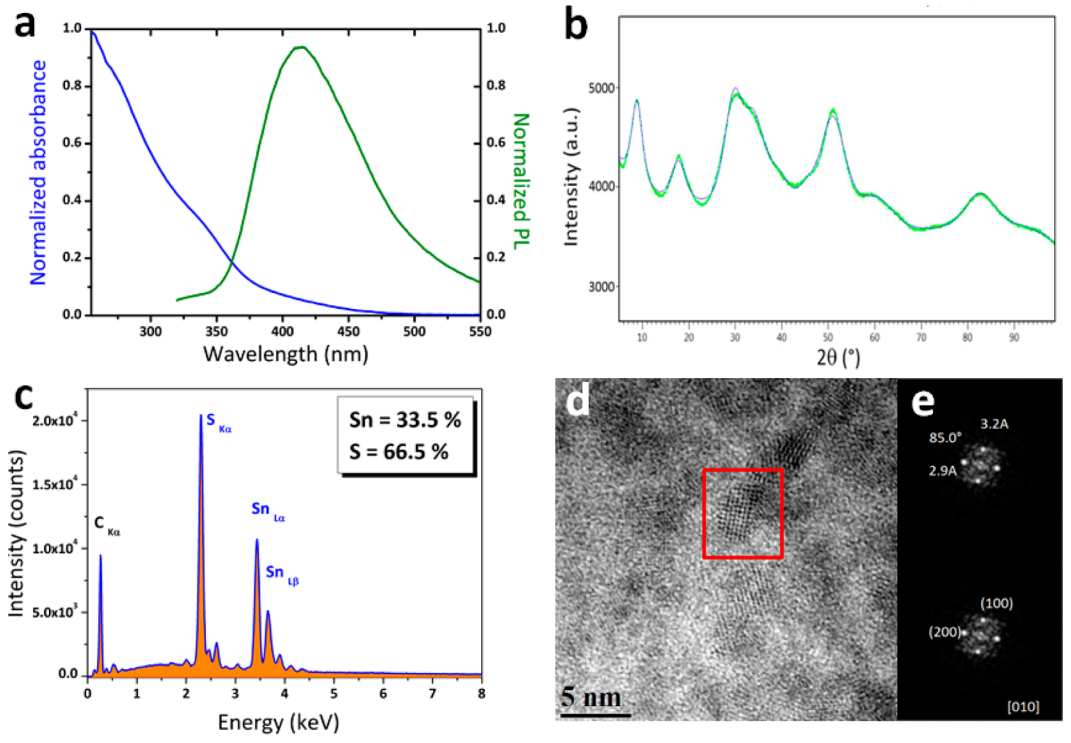

Figure 7. Optical and structural characterization of the 2−3 nm SnS_2 nanoparticles obtained using elemental sulfur/OLA as precursor. (a) UV−vis absorption and photoluminescence spectra. (b) Powder X-ray diffractogram. Green: experimental; blue: LeBail fit of the data assuming space group *P*3*m*1. (c) EDX spectrum. (d) High resolution TEM image. (e) Digital diffraction pattern of the area marked with a square.

we varied the concentrations of the tin and sulfur precursors as well as of the ligands/complexing agents. Reaction temperature was another parameter studied, however, at lower temperatures (130 °C, 140 °C) and higher temperatures (>160 °C) the obtained samples exhibited larger polydispersity. Therefore, 150 °C has been used for all experiments. The concentration of precursors has a marked influence on the morphology of the SnS nanoparticles. In a regime of high concentration ([Sn] = 0.1−0.2 M) square nanoplatelets as shown in Figure 1 with typical dimensions of 7 × 17 nm are obtained. Lowering the concentration to intermediate values ([Sn] = 0.02−0.09 M) yields significantly thinner square nanoplatelets (3−4.5 nm) while the lateral dimension is little affected (14−16 nm). Below concentrations of [Sn] = 0.01 M bimodal particle populations are observed, consisting of nanoplatelets and faceted spherical nanoparticles (cf. Figure 5). In all cases the particle morphology was found to be essentially independent from the Sn:S precursor ratio in the investigated range (5:1 to 1:5), although

DOI: 10.1021/jacs.5b05576
J. Am. Chem. Soc. 2015, 137, 9943−9952

a propensity for the formation of spherical particles was observed for the highest sulfur ratios.

The growth of 2D SnS or SnSe nanostructures generally occurs via one of the following mechanisms: (1) oriented or nonoriented attachment of small nanocrystal building blocks;[49] (2) anisotropic growth induced by the selective blocking of specific crystal facets for growth.[22,41] SnS differs from widely studied II−VI, IV−VI and III−V semiconductor nanocrystals in the way that it adopts a layered GeS-type crystal structure, favoring the formation of 2D nanostructures such as sheets or platelets. The analyses of aliquots taken at short reaction times (Figure 5) indicate that in the present synthetic scheme the controlled assembly of preformed spherical/polyhedral SnS nanoparticles is the predominant mechanism of nanoplatelet formation. When using the experimental conditions resulting in the sample shown in Figure 1b, at short reaction times (<2 min) a larger fraction of 7−8 nm spherical nanoparticles coexist with a smaller fraction of nanocuboids. For longer reaction times (>3 min) the fraction of nanoplatelets becomes prevalent, and after 10 min (cf. Figure 1b) no more spherical nanoparticles can be found. In the case of low precursor concentration (Figure 5, bottom row), the initial stages of reaction are similar, showing the coexistence of spherical polyhedra and nanoplatelets with a thickness corresponding to the diameter of the former. However, here the nanoplatelets exhibit a significant growth of their lateral dimensions, up to >100 nm after 15 min. At the same time a second population of large spherical nanoparticles appears, which are well calibrated in size (mean diameter: 42 nm).

Building on these observations we propose a growth mechanism, during which in the initial stages spherical seed particles are created after injection of the sulfur precursor into the solution of the tin precursor. The spherical nanoparticles self-assemble subsequently to form square nanoplatelets of fixed thickness corresponding to the diameter of the seed particles. A similar growth mechanism has been observed in the case of SnSe nanosheets.[49] At low concentrations, the growth of the seed particles becomes a competing pathway to their assembly in form of nanoplatelets. At the same time the much slower growth under diluted conditions leads to significantly increased lateral dimensions of the nanoplatelets. They can be conveniently separated from the large-sized spherical nanoparticles by means of size-selective precipitation. Figure 6 summarizes the proposed growth mechanism.

3. Use of Elemental Sulfur Instead of TAA: Synthesis of SnS_2 Nanoparticles. When TAA is replaced by elemental sulfur solubilized in OLA as the sulfur source, the synthesis described above yields small (2−3 nm), spherical $Sn^{IV}S_2$ nanocrystals. As expected the tin precursor is not reduced in the absence of H_2S-forming TAA during the second stage of reaction.

Bulk SnS_2 exhibits an indirect band gap of 2.2 eV[28] and by consequence the color of the reaction mixture, which turns black in case of SnS nanoparticles, here evolves from colorless to yellow and finally orange with time. The absorption spectrum (Figure 7a) shows a shoulder at 350 nm and a red tail with an onset at around 470 nm. Contrary to the studied SnS nanoparticles, also a photoluminescence (PL) signal could be detected. The PL peak maximum is situated at 450 nm with a line width of 90 nm (fwhm) and an asymmetry on the larger wavelength side. The deduced optical band gap of 2.8 eV indicates quantum confinement effects. The X-ray diffractogram exhibits broad peaks (Figure 7b), which can be indexed assuming a berndtite 4H crystallographic phase with space group $P3m1$ as identified by Palosz et al.[50] Lattice parameters were inferred from a LeBail fit of the data: a = 3.62(5) Å and c = 10.00(5) Å. We underline that space group $P6_3mc$ is commonly assigned to the 4H polytype of SnS_2, characterized by existence conditions as l = 2n for (00l) reflections. However, in our case the experimental pattern displays two peaks associated with interreticular distances of 10.0(1) and 5.05(5) Å, which can be unambiguously assigned to (001) and (002) reflections, respectively. $P6_3mc$ has therefore to be excluded. According to the Scherrer formula, the widths of the peaks are compatible with 2−3 nm sized nanocrystals. EDX analysis (Figure 7c) confirms the SnS_2 stoichiometry with a Sn:S ratio of 66.3:33.7. SEM imaging was not successful due to the small size of the nanocrystals, and also TEM imaging is complicated as the contrast of the SnS_2 nanoparticles on amorphous carbon substrate is low. Nonetheless it was possible to analyze the size, shape and crystallinity on high-resolution TEM images (Figure 7d,e). The nanocrystals are polymorphous and their mean size is in accordance with that determined from the X-ray data. Furthermore, the analysis of digital diffraction patterns of selected particles confirms the crystalline phase: the mean spots show distances and angles, which are correlated to the presence of (100) and (200) planes of a hexagonal lattice in the space group $P3m1$ ([010] orientation).

SnS_2 has been suggested as potential substitute for CdS in the buffer layer of thin film CIGS (or kesterite) solar cells, combining nontoxicity, stability and low cost due to the large earth abundance of its constituents.[51] Recent DFT calculations predict values of −5.02 eV and −7.30 eV, respectively, for the electron affinity and ionization potential in SnS_2 as well as n-type character due to prevailing S vacancies.[28] To identify the energy levels in our samples, we carried out electrochemical studies on thin films of the obtained SnS_2 nanoparticles (cf. Supporting Information). Differential pulse voltammetry (DPV) reveals a well-defined reduction peak at 0.04 V vs the ferrocene/ferrocenium redox couple, resulting in an electron affinity of −4.8 eV. In accordance with the observed quantum confinement in the optical spectra, the electron affinity is shifted (here by 200 meV) with respect to the bulk, reaching a value close to that measured under the same conditions for 13 nm CdS NCs (−4.6 eV). The possibility of adjusting the electron affinity with the nanoparticle size opens interesting perspectives for the use of SnS_2 as n-type buffer layer in thin film solar cells in terms of optimization of the conduction band offset with respect to the absorber material.

■ CONCLUSION

We present a new method for the synthesis of well-calibrated square SnS nanoplatelets showing comparably small dimensions (thickness 4−15 nm, edge length 15−100 nm) with respect to reported works on SnS 2D nanostructures. An appealing side effect of the small size is the observed long-term colloidal stability (several years in chloroform), a prerequisite for nanoparticles' processing, e.g., in thin films or as additive to polymer matrices. This is of particular interest in view of applying SnS nanoplatelets as light harvesting material in solar cells. Tin tetrachloride pentahydride has been identified as an easy to handle and versatile precursor of SnS nanoplatelets (with thioacetamide), or of small SnS_2 nanoparticles (with elemental sulfur). The crystallographic properties of the nanoplatelets could be precisely related to the morphology by means of electron tomography on single particles. For the first

DOI: 10.1021/jacs.5b05576
J. Am. Chem. Soc. 2015, 137, 9943−9952

time, the internal structure of SnS nanoplatelets has been investigated in details using atomic resolution electron microscopy techniques, combined with simulations of the experimental data. These analyses reveal the presence of Sn vacancy rich (100) planes, while the observed periodic contrast modulations indicate an ordering of these defects. The obtained small SnS_2 nanoparticles exhibit quantum confinement effects and well-passivated surface states as confirmed by the measurement of their photoluminescence spectrum. The electronic energy levels of SnS_2 nanoparticles determined from electrochemical and optical studies place them as potential candidate for substituting toxic CdS as buffer material in thin film solar cells.

■ ASSOCIATED CONTENT

Supporting Information

The Supporting Information is available free of charge on the ACS Publications website at DOI: 10.1021/jacs.5b05576.

Size distributions of nanoplatelets, ESI mass spectrum of reaction intermediate, EDX data, UV−vis absorption spectra of SnS nanoplatelets, electrochemical measurements of SnS_2 and CdS nanoparticles. (PDF)

■ AUTHOR INFORMATION

Corresponding Authors

*antoine@dekergommeaux.com

*peter.reiss@cea.fr

Present Address

⊗Solvay Research and Innovation Center of Paris, 52 rue de la Haie Coq, 93000 Aubervilliers, France.

Notes

The authors declare no competing financial interest.

■ ACKNOWLEDGMENTS

This research was supported by the Micro-Nano and Energy research clusters of the Region Rhônes-Alpes. M.L.H. acknowledges access to the Minatec nanocharacterization facility PFNC and financial support from the CEA "Programme Transverse Nanosciences" (project TOMOENER), from Eurotalents, which is funded by CEA and the Marie Curie Actions of the European Commission, and from the MECD Spanish Ministry (ref EX2010-1135). The authors thank Dr. Pascale Bayle-Guillemaud (CEA-INAC/SP2M), Dr. Axel Maurice (CEA-INAC/SPrAM) and Dr. Jacky Even (FOTON Univ. Rennes) for helpful discussions.

■ REFERENCES

(1) Kumar, S.; Nann, T. *Small* **2006**, *2*, 316.

(2) Manna, L.; Milliron, D. J.; Meisel, A.; Scher, E. C.; Alivisatos, A. P. *Nat. Mater.* **2003**, *2*, 382.

(3) Deka, S.; Miszta, K.; Dorfs, D.; Genovese, A.; Bertoni, G.; Manna, L. *Nano Lett.* **2010**, *10*, 3770.

(4) Gur, I.; Fromer, N. A.; Chen, C. P.; Kanaras, A. G.; Alivisatos, A. P. *Nano Lett.* **2007**, *7*, 409.

(5) Vaughn Ii, D. D.; Patel, R. J.; Hickner, M. A.; Schaak, R. E. *J. Am. Chem. Soc.* **2010**, *132*, 15170.

(6) Ithurria, S.; Tessier, M. D.; Mahler, B.; Lobo, R. P. S. M.; Dubertret, B.; Efros, A. L. *Nat. Mater.* **2011**, *10*, 936.

(7) Son, J. S.; Yu, J. H.; Kwon, S. G.; Lee, J.; Joo, J.; Hyeon, T. *Adv. Mater.* **2011**, *23*, 3214.

(8) Ithurria, S.; Bousquet, G.; Dubertret, B. *J. Am. Chem. Soc.* **2011**, *133*, 3070.

(9) Zhang, S.-Y.; Regulacio, M. D.; Han, M.-Y. *Chem. Soc. Rev.* **2014**, *43*, 2301.

(10) Rossitto, E.; Lecarme, O.; Latu-Romain, L.; Berton, K.; Pinedo-Rivera, T.; Jiu, T.; Reiss, P.; Peyrade, D. *Microelectron. Eng.* **2009**, *86*, 828.

(11) Zanella, M.; Gomes, R.; Povia, M.; Giannini, C.; Zhang, Y.; Riskin, A.; Van Bael, M.; Hens, Z.; Manna, L. *Adv. Mater.* **2011**, *23*, 2205.

(12) Baranov, D.; Fiore, A.; van Huis, M.; Giannini, C.; Falqui, A.; Lafont, U.; Zandbergen, H.; Zanella, M.; Cingolani, R.; Manna, L. *Nano Lett.* **2010**, *10*, 743.

(13) Sun, B.; Sirringhaus, H. *J. Am. Chem. Soc.* **2006**, *128*, 16231.

(14) Chiu, S.-C.; Jhang, J.-S.; Lin, Y.-F.; Hsu, S.-Y.; Fang, J.; Jian, W.-B. *Nanoscale* **2013**, *5*, 8555.

(15) Persano, A.; De Giorgi, M.; Fiore, A.; Cingolani, R.; Manna, L.; Cola, A.; Krahne, R. *ACS Nano* **2010**, *4*, 1646.

(16) Park, H. H.; Heasley, R.; Sun, L.; Steinmann, V.; Jaramillo, R.; Hartman, K.; Chakraborty, R.; Sinsermsuksakul, P.; Chua, D.; Buonassisi, T.; Gordon, R. G. *Prog. Photovoltaics* **2015**, *23*, 901.

(17) Alexandros, S.; Jason, M. S.; Christopher, A. C.; Andrew, G. C.; Patrick, S. G.; Andrew, A. R. W. *Nanotechnology* **2010**, *21*, 185202.

(18) Deng, Z.; Cao, D.; He, J.; Lin, S.; Lindsay, S. M.; Liu, Y. *ACS Nano* **2012**, *6*, 6197.

(19) Chao, J.; Wang, Z.; Xu, X.; Xiang, Q.; Song, W.; Chen, G.; Hu, J.; Chen, D. *RSC Adv.* **2013**, *3*, 2746.

(20) Vaughn, D. D.; Hentz, O. D.; Chen, S.; Wang, D.; Schaak, R. E. *Chem. Commun.* **2012**, *48*, 5608.

(21) Tripathi, A. M.; Mitra, S. *RSC Adv.* **2014**, *4*, 10358.

(22) Lu, J.; Nan, C.; Li, L.; Peng, Q.; Li, Y. *Nano Res.* **2013**, *6*, 55.

(23) Bhattacharya, S.; Gunda, N. S. H.; Stern, R.; Jacobs, S.; Chmielowski, R.; Dennler, G.; Madsen, G. K. H. *Phys. Chem. Chem. Phys.* **2015**, *17*, 9161.

(24) Sharon, M.; Basavaswaran, K. *Sol. Cells* **1988**, *25*, 97.

(25) Vidal, J.; Lany, S.; d'Avezac, M.; Zunger, A.; Zakutayev, A.; Francis, J.; Tate, J. *Appl. Phys. Lett.* **2012**, *100*, 032104.

(26) Koteswara Reddy, N.; Ramakrishna Reddy, K. T. *Thin Solid Films* **1998**, *325*, 4.

(27) Sinsermsuksakul, P.; Sun, L.; Lee, S. W.; Park, H. H.; Kim, S. B.; Yang, C.; Gordon, R. G. *Adv. Energy Mater.* **2014**, *4*, 1400496.

(28) Burton, L. A.; Colombara, D.; Abellon, R. D.; Grozema, F. C.; Peter, L. M.; Savenije, T. J.; Dennler, G.; Walsh, A. *Chem. Mater.* **2013**, *25*, 4908.

(29) de Kergommeaux, A.; Faure-Vincent, J.; Pron, A.; de Bettignies, R.; Reiss, P. *Thin Solid Films* **2013**, *535*, 376.

(30) Walsh, A.; Watson, G. W. *J. Phys. Chem. B* **2005**, *109*, 18868.

(31) Xu, Y.; Al-Salim, N.; Bumby, C. W.; Tilley, R. D. *J. Am. Chem. Soc.* **2009**, *131*, 15990.

(32) Hickey, S. G.; Waurisch, C.; Rellinghaus, B.; Eychmuller, A. *J. Am. Chem. Soc.* **2008**, *130*, 14978.

(33) Biacchi, A. J.; Vaughn, D. D.; Schaak, R. E. *J. Am. Chem. Soc.* **2013**, *135*, 11634.

(34) de Kergommeaux, A.; Faure-Vincent, J.; Pron, A.; de Bettignies, R.; Malaman, B.; Reiss, P. *J. Am. Chem. Soc.* **2012**, *134*, 11659.

(35) Deng, Z.; Han, D.; Liu, Y. *Nanoscale* **2011**, *3*, 4346.

(36) Ning, J.; Men, K.; Xiao, G.; Wang, L.; Dai, Q.; Zou, B.; Liu, B.; Zou, G. *Nanoscale* **2010**, *2*, 1699.

(37) Zhang, H.; Hyun, B.-R.; Wise, F. W.; Robinson, R. D. *Nano Lett.* **2012**, *12*, 5856.

(38) Koktysh, D. S.; McBride, J. R.; Geil, R. D.; Schmidt, B. W.; Rogers, B. R.; Rosenthal, S. J. *Mater. Sci. Eng., B* **2010**, *170*, 117.

(39) Greyson, E. C.; Barton, J. E.; Odom, T. W. *Small* **2006**, *2*, 368.

(40) Patra, B. K.; Sarkar, S.; Guria, A. K.; Pradhan, N. *J. Phys. Chem. Lett.* **2013**, *4*, 3929.

(41) Liu, X.; Li, Y.; Zhou, B.; Wang, X.; Cartwright, A. N.; Swihart, M. T. *Chem. Mater.* **2014**, *26*, 3515.

(42) Bernal, S.; Botana, F. J.; Calvino, J. J.; López-Cartes, C.; Pérez-Omil, J. A.; Rodríguez-Izquierdo, J. M. *Ultramicroscopy* **1998**, *72*, 135.

(43) Kirkland, E. J. *Advanced Computing in Electrons Microscopy*, 2nd ed.; Springer: New York, 2010.

DOI: 10.1021/jacs.5b05576
J. Am. Chem. Soc. 2015, 137, 9943−9952

(44) Wiedemeier, H.; Schnering, H. G. v. *Zeitschrift für Kristallographie* **1978**, *148*, 295.
(45) Rodríguez-Carvajal, J. *Comm. Powder Diffr. Newsl.* **2001**, *26*, 12.
(46) Pennycook, S. J.; Boatner, L. A. *Nature* **1988**, *336*, 565.
(47) Zuo, J.-M.; Shah, A. B.; Kim, H.; Meng, Y.; Gao, W.; Rouviére, J.-L. *Ultramicroscopy* **2014**, *136*, 50.
(48) Semenov, S. N.; Maltsev, E. Y.; Timokhin, I. G.; Drozdov, A. A.; Troyanov, S. I. *Mendeleev Commun.* **2005**, *15*, 205.
(49) Vaughn, D. D.; In, S.-I.; Schaak, R. E. *ACS Nano* **2011**, *5*, 8852.
(50) Palosz, B.; Steurer, W.; Schulz, H. *Acta Crystallogr., Sect. B: Struct. Sci.* **1990**, *B46*, 449.
(51) Hariskos, D.; Spiering, S.; Powalla, M. *Thin Solid Films* **2005**, *480−481*, 99.

DOI: 10.1021/jacs.5b05576
J. Am. Chem. Soc. 2015, 137, 9943−9952